Polymer 356 (2026) 129963

Contents lists available at ScienceDirect

Polymer

journal homepage: www.elsevier.com/locate/polymer

Nanoscale organization, thermal properties, and encapsulation performance of star-shaped poly(L-Lactide): Effect of glycerol- and diglycerol-based core geometry

Benedetta Brugnoli [a], Chiara Frezza [a,b], Alessia Mariano [c,d], Philippa L. Jacob [e], Andreas Diacono [f], Derek Irvine [f], Eleni Axioti [e], Alessandra Del Giudice [a], Luciano Galantini [a], Antonella Piozzi [a], Anna Scotto d'Abusco [c], Vincenzo Taresco [e,*], Iolanda Francolini [a,**]

[a] Department of Chemistry, Sapienza University of Rome, P.le Aldo Moro 5, Rome, Italy
[b] Department of Industrial, Electronic and Mechanical Engineering, Roma Tre University, Via Vito Volterra 62, Rome, Italy
[c] Department of Biochemical Sciences, Sapienza University of Rome, P.le Aldo Moro 5, Rome, Italy
[d] BeSSA Department of Wellbeing, Health and Environmental Sustainability, Sapienza University of Rome, Rieti, Italy
[e] School of Chemistry, University of Nottingham, NG7 2RD, Nottingham, UK
[f] Centre for Additive Manufacturing, Faculty of Engineering, University of Nottingham, Nottingham, NG7 2RD UK

ARTICLE INFO

Keywords:
Star-shaped poly-L-lactide
Hydrophobic molecule encapsulation
Core geometry
MDA-MB-231 breast cancer cells
Usnic acid

ABSTRACT

Single-point star-shaped poly(L-lactide) (PLLA) architectures are here synthesized using bio-sourced glycerol and diglycerol as polyfunctional initiators, to investigate the influence of polymer topology and core geometry on nanoscale organization, thermal behavior, and encapsulation of hydrophobic probes. NMR spectroscopy confirmed the branched structure while SAXS revealed architecture-dependent chain conformations in solution, with a transition from single-chain behavior to lamellar aggregation as branching and molar mass increased. Star-shaped PLLA generally showed amorphous behavior and lower thermal stability than linear PLLA. However, in the diglycerol series, increasing arm length induced semicrystalline behavior, attributed to steric constraints at the core that promote asymmetric arm growth and favor extended chains in spatially separated arms. Nanoprecipitation in water yielded nanoaggregates (ca. 200 nm in size) displaying colloidal stability up to 1 month. Encapsulation studies using usnic acid as a hydrophobic probe highlighted architecture-driven effects on amount and physical state of encapsulated compound. Diglycerol core promoted amorphous guest stabilization, suggesting that encapsulation is dictated by core-controlled arm growth and packing. Cytotoxicity assays in MDA-MB-231 triple-negative breast cancer cells showed that UA encapsulation in diglycerol-based star-shaped PLLA reduces cytotoxicity and integrin β1 expression, supporting the system's ability to control interfacial interactions at the bio–nano interface.

1. Introduction

The design of advanced macromolecular architectures has become a central theme in modern polymer physics and chemistry, as it enables precise control over molecular organization, chain dynamics, and solution behavior [1,2]. In this context, the transition from simple linear chains to branched and hierarchical topologies represents a significant step forward in tailoring polymer properties at multiple length scales [2,3].

Among branched architectures, single point star-shaped polymers constitute a distinctive class due to their compact and globular conformation. Thanks to their tunable branch length and number, they exhibit unique crystallization behavior and rheological properties [4,5], arising from constrained chain conformations and reduced entanglement density affecting nanoscale packing and domain formation. The multi-arm topology also concentrates a high density of end-group functionalities

This article is part of a special issue entitled: EPF-2025: Future Faculty published in Polymer.

* Corresponding author.
** Corresponding author.
E-mail addresses: vincenzo.taresco@nottingham.ac.uk (V. Taresco), iolanda.francolini@uniroma1.it (I. Francolini).

https://doi.org/10.1016/j.polymer.2026.129963
Received 30 January 2026; Received in revised form 20 March 2026; Accepted 2 April 2026
Available online 6 April 2026
0032-3861/© 2026 The Authors. Published by Elsevier Ltd. This is an open access article under the CC BY license (http://creativecommons.org/licenses/by/4.0/).

within a confined volume, strongly influencing interfacial interactions and self-assembly [1]. These features make star-shaped polymers particularly attractive for the encapsulation of hydrophobic molecules [6,7], as they may favor the formation of confined hydrophobic domains, and tunable interfacial organization, which are crucial for efficient guest accommodation and stabilization in hydrophilic environments. The ability to encapsulate hydrophobic guest molecules, including drugs, fluorescent probes, lipophilic additives, or functional agents, not only serves as a functional indicator of chain packing and core compactness but is, also, a key property for the design of polymeric materials for solubilization and formulation across diverse applications, such as drug delivery, packaging, and coatings.

Among star-shaped polymers, poly(L-lactide) (PLLA) is a valuable model system due to its semicrystalline nature and architecture-dependent chain packing [8,9]. Several studies have shown that increasing the degree of branching in star-shaped PLLA significantly affects its crystallization behavior. Tsuji et al. [10] compared 3-arm PLLAs (Mn = 13–63 kg/mol) with linear counterparts and highlighted that branching restricts segmental mobility and promotes exclusion of chain segments from crystalline regions. Hao et al. [11] demonstrated that, for PLLAs with Mn around 35 kg/mol, an increase in the number of arms up to six leads to a progressive reduction in both the nonisothermal crystallization peak temperature (Tc) and the overall isothermal crystallization rate, indicating a clear retardation of crystallization kinetics induced by architectural complexity. Biela et al. [12] reported the synthesis of star-shaped poly(L-lactide)s bearing variable numbers of secondary hydroxyl groups at linear arms chain-ends and primary hydroxyl groups directly attached to dipentaerithritol core. Characterization by SEC, NMR, MALDI-TOF demonstrated that the number of arms significantly affects chromatographic elution behavior under critical conditions, confirming well-defined star architectures and revealing architecture-dependent solution behavior. Further insight was provided by Sakamoto and Tsuji [13], who studied 4-arm PLLAs over a broad molecular weight range (Mn = 6.9–98 kg/mol). Their results showed that star architecture alters both crystallization pathways and the transition between α′ and α crystalline forms. Compared with linear PLLA, branched structures were found to delay or suppress both cold and isothermal crystallization processes, with thermal parameters and crystal morphology strongly influenced by molecular weight per arm.

Despite these advances in understanding crystallization and thermal behavior, only a limited number of studies have explored the use of star-shaped PLLA architectures for the encapsulation of hydrophobic compounds, particularly drug molecules. Reported examples include camptothecin loaded into three-arm PLLA blocks [14], curcumin in four-arm PLLA porous microspheres [15] and atorvastatin in four-arm PDLA structures [16]. However, a fundamental understanding of how key structural parameters, such as the number and length of polymer arms, as well as core geometry and flexibility, govern nanoscale organization and guest molecule encapsulation remains largely unexplored.

In this work, linear and star-shaped PLLA architectures were synthesized via ring opening polymerization (ROP) of L-lactide using both mono- and polyfunctional bio-sourced polyalcohol initiators, glycerol and diglycerol. The use of glycerol and diglycerol allows the preparation of discrete, flexible cores while simultaneously introducing environmentally favorable materials [17].

Our choice of glycerol and diglycerol as initiators was deliberate, as both are bio-derived polyols, glycerol being a major by-product of the biodiesel industry, and their use aligns with our goal of developing a sustainable and biocompatible library of amphiphilic PLLA-based materials. Beyond this sustainability motivation, the different chemical structures of glycerol and diglycerol introduce variations in the number and type of hydroxyl groups (primary vs secondary) that participate in the ring-opening polymerization, which can influence initiation efficiency, polymer architecture, and ultimately the physicochemical properties of the resulting materials.

The influence of macromolecular architecture on fundamental properties was investigated using NMR spectroscopy, gel permeation chromatography (GPC), small-angle X-ray scattering (SAXS), differential scanning calorimetry (DSC) and thermogravimetric analysis (TGA). Self-assembly in water and colloidal stability were further assessed by dynamic light scattering (DLS), also in the presence of a hydrophobic probe molecule, usnic acid (UA), to evaluate the effects of architecture, core geometry and arm length, on polymer encapsulation behavior. Since UA is a chemotherapy agent against solid tumors [18], with high hepatotoxic effects limiting its administration [19], *in vitro* cytotoxicity assays were performed on UA-encapsulated systems using triple-negative breast cancer cells, MDA-MB-231, as a complementary indicator of architecture-dependent interfacial behavior, exploring its advantage compared to free UA.

2. Materials and methods

2.1. Materials

L-lactide (L-LA) was kindly supplied from Corbion. Glycerol (Gly), benzyl alcohol (BA) 1,8-diazabicyclo(5.4.0)undec-7-ene (DBU), benzoic acid (BAc), usnic acid (UA) and sodium sulphate (Na_2SO_4) were bought from Sigma Aldrich. 3,3′-oxybis(propane-1,2-diol) or diglycerol (DGly) was supplied by BLDpharm. All the reagents were used as received.

2.2. Synthesis of linear and star-shaped polyol-based polyesters

Linear and star-shaped PLLA were synthesized by ROP by using mono and polyfunctional polyols (Scheme 1). For linear PLLA, L-LA (2.5 g, 17 mmol) and BA (0.076 g, 0.71 mmol) were solubilized in anhydrous dichloromethane (DCM, 20 mL), using a [M]/[I] = 24. The catalyst DBU (30 μ L, 0.2 mmol) was then added. After 24 h polymerization, the mixture was quenched by adding BAc (0.03 g, 0.24 mol). The product was then purified by liquid-liquid extraction in a separator funnel by washing the organic solution with cold water. The latter was further washed with DCM to recover the product. Finally, the organic mixture was dried over anhydrous Na_2SO_4 and the solvent was evaporated under vacuum.

A series of star-shaped polymers with different arm lengths was obtained under reaction conditions analogous to those employed for linear PLLA by varying the [M]/[I] ratios to 8, 16, and 24. After purification and recovery, polymer powders were kept in the freezer. Samples were named Gly/DGly-PLLA*n* where *n* is the [M]/[I] ratio (8, 16 or 24). Also, Gly-PDLLA4 was synthesized as a model for characterisation purposes with an alternative purification method performed by precipitation into a cold 50:50 (v/v) mixture of diethyl ether and petroleum ether (40–60 °C fraction, 40 mL). The precipitate was collected by centrifugation (4000 rpm, 10 min), the supernatant was decanted, and the residue was dried under vacuum to afford the final oligomer.

2.3. Spectroscopy

Successful polymerization and repeat unit analysis were characterized by ^{1}H and ^{13}C NMR and 2D NMR spectroscopy. Monomers and polymers were solubilized in deuterated chloroform ($CDCl_3$) and were analysed using a Bruker Avance 400 spectrometer operating at 400 MHz (^{1}H) and 101 MHz (^{13}C), assigning chemical shifts in parts per million (ppm). NMR spectra were referenced to 7.26 ppm for ^{1}H NMR spectroscopy and 77.16 ppm for ^{13}C NMR spectroscopy in $CDCl_3$. HSQC, HMBC and COSY experiments were acquired to assist with structural assignment. MestReNova 15.0.0 copyright 2023 (Mestrelab Research S. L.) was used for analysing the spectra.

The experimental degree of polymerization ($DP_{n,\mathrm{exp}}$) was obtained by the integration of the proton signal from the end-group ($I_{CH,end-group}$) at 4.5 ppm vs integration of the proton signal from the polymer repeating unit (I_{CH}) at 5.2 ppm, according to the following equation:

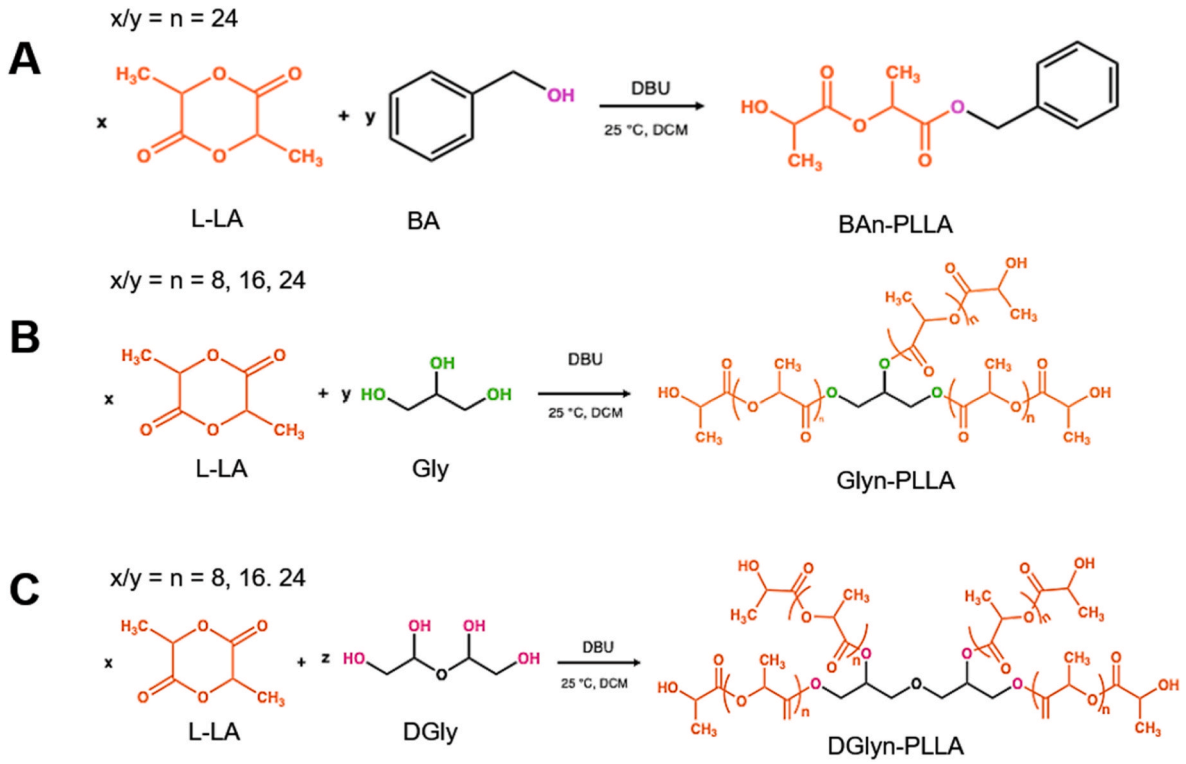

Scheme 1. Synthesis of linear (A) and star-shaped PLLA (B and C).

$$DP_{n,exp} = \frac{(I_{CH} + I_{CH,end-group})}{I_{CH,end-group}}$$

The number-average molar mass ($M_{n,NMR}$) of the polymers was obtained from the $DP_{n,exp}$ by considering that all the OH groups of the initiator started the polymerization, as follow:

$$M_{n,NMR} = M_{In} + (M_{LA} x DP_{n,exp})\ x\ (n\ OH\ groups\ in\ the\ initiator)$$

where M_{In} is the molar mass of the initiator and M_{LA} is the molar mass of the L-lactide.

For each polymer, the monomer conversion yield was calculated as the ratio between the experimental (*DPn,exp*) and theoretical (*DPn,th*) degree of polymerization, as follow:

$$conversion = \frac{DP_{n,exp}}{DP_{n,th}}\ x\ 100$$

2.4. Gel permeation chromatography (GPC)

Measurements were performed in THF (HPLC grade, Fisher Scientific) as the eluent at 40 °C using two Agilent PL-gel mixed-D columns in series, an injection loop of 50 μL, with a flow rate of 1 mL/min. Each polymer solution (3 mg/mL) was filtered in 0.22 μm Teflon filter. A differential refractomer (DRI) was used for the detection of samples. The system was calibrated using poly(methyl methacrylate) standards with average molar mass in the range from 540 to $1.02 \cdot 10^6$ g/mol and dispersity (*Đ*) close to 1.0.

2.5. Small angle X-ray scattering (SAXS)

SAXS analysis was performed on polymer solutions (10 mg/mL) in acetone for all polymers (Fig. S10 and Table S1), except for Gly-PLLA24 and DGly-PLLA24. In this case, THF was used due to solubility limitations in acetone. The X-ray scattering measurements were performed at SAXSLab Sapienza with a Xeuss 2.0 Q Xoom system (Xenocs SAS, Grenoble, France) equipped with a micro-focus Genix 3D X-ray Cu source (λ = 0.1542 nm) and a two-dimensional Pilatus3 R 300 K detector placed at a variable distance from the sample (Dectris Ltd., Baden, Switzerland). The beam size was defined through the two-pinhole collimation system equipped with "scatterless" slits to be 0.5 mm × 0.5 mm. Calibration of the scattering vector modulus q range, where $q = (4\pi \sin\theta)/\lambda$, 2θ being the scattering angle, was performed using silver behenate. The solutions of the polymers dissolved in acetone or THF (10 mg/mL) were loaded into disposable borosilicate glass capillaries and sealed with hot glue. Measurements were performed at room temperature (25 ± 1 °C) and at reduced pressure (<0.2 mbar). Two sample-detector distances (550 mm and 2500 mm) were employed so that the available q range was 0.042-6.0 nm^{-1}. The two-dimensional scattering patterns were subtracted for the "dark" counts, and then masked, azimuthally averaged, and normalized for transmitted beam intensity, exposure time, and subtended solid angle per pixel, by using the FoxTrot software developed at SOLEIL. The one-dimensional intensity vs. q profiles were subtracted for the contributions of the empty capillary and the solvent (acetone or THF) and put in intensity units of macroscopic scattering cross-section (cm^{-1}) by dividing for the capillary thickness estimated from the alignment scans. Model calculations of scattering profiles were performed using the software SasView [SasView version 5.0.2, (n.d.). http://www.sasview.org/(accessed September 7, 2019)]. To get an indication of the size in the real space of the inhomogeneities giving rise to the SAXS profiles, pair distance distribution functions were obtained by indirect Fourier inversion using the software GNOM of the ATSAS package [20].

2.6. Thermal analysis

Thermal stability of polymers was assessed by a TG 50 balance equipped with a TC 10 A processor. The explored temperature range was 25-600 °C at a scan rate of 10 °C/min, under nitrogen flow (25 mL/min) on sample weight of ca. 5-7 mg.

Differential scanning calorimetry (DSC) was performed by using a calorimeter Mettler Toledo DSC 822e. The temperature program was the

following: i) first heating scan from 25 to 210 °C, ii) cooling scan until −70 °C, and iii) a second heating scan from −70 to 210 °C. All the scans were conducted at a heating rate of 10 °C/min, under a nitrogen atmosphere with a flow rate of 30 mL/min. Degree of crystallinity (χ_c) was calculated using the following equation:

$$\chi_c(\%) = \frac{\Delta H_m}{\Delta H_m^0} x100$$

where ΔH_m^0 is the theoretical melting enthalpy of a 100% crystalline PLLA (93.7 J/g) [21,22].

2.7. Polarized optical microscopy (POM)

The morphology and isothermal growth rates of star-shaped PLLA were investigated by POM using a Nikon Optiphot2-Pol microscope equipped with a Linkam HFS 91 hot stage and a Nikon D7200 digital camera. To ensure a reproducible initial state, samples were melted between two glass slides at 200 °C and held for 5 min to erase the thermal history. Subsequently, samples were cooled at 20 °C/min to the crystallization temperature (T_c = 125 °C) for isothermal analysis.

2.8. Polymer assembly in water

Polymer assembly was induced in water by nanoprecipitation using THF and acetone as co-solvents for the polymer, as previously reported [23]. Each polymer (5 mg) was solubilized in THF (1 mL). Then, acetone (2 mL) was added to obtain a 1.7 mg/mL final concentration. The resulting solution (3 mL) was added dropwise into DI water (10 mL), under controlled stirring (250 rpm) and left overnight to let the solvent evaporate.

Hydrodynamic size, polydispersity index (PDI), and ζ-potential of obtained nanosystems were determined by using a Zetasizer Nano apparatus (Malvern Instruments Ltd., Malvern, UK) equipped with a 4 mW HeNe laser source (632.8 nm). The measurements were carried out at 25 °C using a folded capillary zeta cell (DTS1070).

2.9. Polymer encapsulation ability

The encapsulation properties of star-polymers were assessed by using UA, as a probe molecule. For UA encapsulation, UA (1 mg) was dissolved in acetone (2 mL) and added to polymer solution (1.7 mg/mL) in THF and acetone mixture. The drug/polymer solution was then added dropwise into DI water (10 mL) under controlled stirring (250 rpm) and left overnight to let the solvent evaporate.

The amount of encapsulated UA was assessed by UV-vis spectroscopy, through the determination of UA apparent solubility, as previously described [24]. Particularly, absorbance of the free UA (A_0) and of the aqueous solutions of UA-loaded polymer systems (A) was measured at 290 nm, using the unloaded-polymer solutions as a blank. All measured absorbance values were kept within the linear range of the Beer–Lambert law (0 < A < 1) to ensure a direct and valid correlation between absorbance and drug concentration. The variation in apparent water solubility (ΔA%) was quantified as follow:

$$\Delta A\% = \frac{(A - A_0)}{A_0} \times 100$$

The UA-encapsulated systems were also characterized by DLS, to assess variation in hydrodynamic size, polydispersity index (PDI), and ζ-potential compared to plain systems. DSC was performed to evaluate the percentage of amorphous drug relative to the total entrapped drug according to the following equation:

$$amorphous\ UA(\%) = \frac{\Delta H_c}{\Delta H_m} \times 100$$

where ΔH_c and ΔH_m are the crystallization and melting enthalpies of UA, respectively.

2.10. Field emission scanning electron microscopy (FESEM)

The morphology of lin-PLLA24, Gly-PLLA24 and DGly-PLLA24 nanoaggregates was observed using high resolution FESEM (AURIGA Zeiss). Each suspension (10 μL) was deposited on a piece of silicon chip. After taken off the excess, the deposited layer was washed several time with water. Before the analysis, each suspension was sputtered with gold layer of 20 nm.

2.11. Biological tests

The human triple-negative breast cancer cell line MDA-MB-231 was obtained from American Type Culture Collection (ATCC; HTB-26, Rockville, MD, USA) and used for biological analyses. Cells were cultured in low-glucose Dulbecco's Modified Eagle Medium (DMEM; Sigma-Aldrich) supplemented with 10% fetal bovine serum (FBS; Gibco, Thermo Fisher Scientific, Waltham, MA, USA), 1% penicillin/streptomycin, 1% L-glutamine, and 1% sodium pyruvate (Sigma-Aldrich). Cells were maintained at 37 °C in a humidified atmosphere containing 5% CO_2. The cytotoxic effects of plain and UA-loaded polymers were evaluated using an MTS-based colorimetric assay 3-[4,5-dimethylthiazol-2-yl]-5-[3-carboxymethoxyphenyl]-2-[4-sulfophenyl]

-2H-tetrazolium; Promega Corporation, Madison, WI, USA). MDA-MB-231 cells were seeded at a density of 5 × 10^3 cells per well and left untreated (CTL) or treated with UA or DGly-PLLA24_UA at UA concentrations of 58, 29, and 15 μM for 24 h. Empty DGly-PLLA24 systems were also tested at concentrations corresponding to those of the UA-loaded ones. At each time point, 100 μL of MTS solution was added to each well, and the plates were incubated for 3 h. Absorbance was measured at 492 nm using a microplate reader (NB-12-0035, NeBiotech, Holden, MA, USA).

2.11.1. Immunofluorescence analysis

Integrin β1 proteins were visualized by immunofluorescence. MDA-MB-231 cells were plated at a density of 5 × 10^3/cm^2. The day after seeding, cells were left untreated (CTL) or treated with UA or DGly-PLLA24_UA at UA concentrations of 15 μM for 3 and 24 h. Empty DGly-PLLA24 systems were also tested at a concentration corresponding to that of the UA-loaded ones. Cells were fixed in ethanol for 15 min at room temperature (RT), and visualized with 0.5% Triton-X 100 in PBS for 10 min at RT. Then, cellular proteins were blocked with 3% bovine serum albumin in PBS for 30 min, and cells were incubated for 1 h with anti-Integrin β1 (1:100) primary antibody (Santa Cruz Biotechnology, Dallas, Texas, USA). Cells were washed with PBS and then incubated with Alexa Fluor 595 donkey anti-rabbit red secondary antibody (Invitrogen, Thermo Fisher Scientific, Waltham, MA, USA) (1:400 dilution) for 1 h. Cells were washed and then stained with DAPI to visualize the nuclei. All these steps were performed at RT. The images were captured by a Leica DM IL LED optical microscope, using an AF6000 modular microscope (Leica Microsystem, Milan, Italy).

2.11.2. Densitometric analysis

The free software ImageJ v1.54p (https://imagej.nih.gov/ij/, accessed on 1 March 2024) was used to perform densitometric analysis of protein expression. For each cell culture condition, the integrated red fluorescence density values obtained in immunofluorescence experiments were measured in 50 fields of the captured pictures using the same parameters of exposition, gain and saturation, subtracting the fluorescence of background.

2.12. Statistical analysis

All data were collected from a minimum of three independent experiments, with each experiment conducted in duplicate or triplicate.

Statistical analysis of biological tests was performed using Prism 5.0 software (GraphPad Software, San Diego, CA, USA). Data distribution was evaluated for deviations from normality, and then two-way repeated measures ANOVA followed by Bonferroni post hoc tests were applied to evaluate differences between groups. A *p*-value of less than 0.05 was considered statistically significant.

3. Results and discussion

This work focuses on establishing the effect of Gly- and DGly-based core geometry in star-shaped PLLA on ability to encapsulate hydrophobic guest compounds. Thermal properties and self-assembly behavior in water were also investigated. The encapsulation capability is highly relevant for material-oriented applications, including drug delivery and compatibilization of hydrophobic compounds in polymeric systems.

To investigate this, linear and single-point star-shaped polymers were synthesized via ROP of LLA using DBU as the catalyst and glycerol- and diglycerol as the intiators. Compared to tin(II) octoate, DBU provides a metal-free and more sustainable catalytic route for ROP, enabling polymerization at lower temperatures while avoiding residual metal contamination [25].

3.1. Synthesis of star-shaped PLLA polymers based on glycerol and diglycerol

The success of the polymerization and branching were confirmed by NMR spectroscopy. In Fig. 1, as an example, the ^{1}H NMR spectra of Gly-PLLA8 and DGly-PLLA8 are reported.

Each spectrum exhibited the characteristic peaks of PLLA, including the methyl group at 1.6 ppm (3H), the methine group at 5.2 ppm (1H). The peak located at 4.5 ppm is related to the methine group of end-groups (Fig. 1A and B). These listed peaks demonstrated a downfield shift compared to L-LA monomer confirming the polymerization occurrence (Fig. S1). Furthermore, the CH_2 and CH signals originating from the glycerol and diglycerol cores showed significant shifts, consistent with previously reported data [26].

Coherently with ^{1}H NMR spectra, ^{13}C NMR spectra of the same polymers, Gly-PLLA8 and DGly-PLLA8 (Fig. 1C and D), show peaks at 16.71 and 69.11 ppm attributable to the methyl and methine groups, while the peak at 170 ppm is related to the carbonyl group of the main chain. The presence of 1,2,3-trisubstituted glyceride moieties associated with the branching points of the star-shaped PLLA was indicated by the signal at 69.79 ppm (5.33 ppm in the ^{1}H NMR spectrum, indicative of the 1,2,3-trisubstituted methine proton). Also, a peak at 62.60 ppm, indicative of a glycerol methylene moiety was observed (Fig. S2). As the polymer molar mass increases, these resonances become progressively less distinguishable from the noise due to the decreasing relative contribution of the core with respect to the polymer arms.

A model reaction performed at a lower monomer:initiator (Gly) ratio of 4:1 was analysed by ^{1}H NMR (Fig. S3), ^{13}C NMR (Fig. S4), HMBC NMR (Fig. S5), COSY NMR (Fig. S6) and HSQC NMR (Figs. S7 and S8). HMBC NMR spectroscopy (Fig. S5) revealed a correlation of the 1,2,3-trisubstituted glyceride methine peak at 69.79 ppm with one at 62.60 ppm, indicative of a glycerol methylene moiety, confirming the presence of the 1,2,3-trisubstitution. Furthermore, in the model reaction, the presence of peaks at 65.56 and 67.51 ppm were observed, indicative of the glycerol methylene and methine protons respectively of the 1,3-disubstituted glyceride species (Fig. S4), a precursor to the 1,2,3-trisubstituted glyceride. This peak, indicative of the 1,3-disubstituted species was

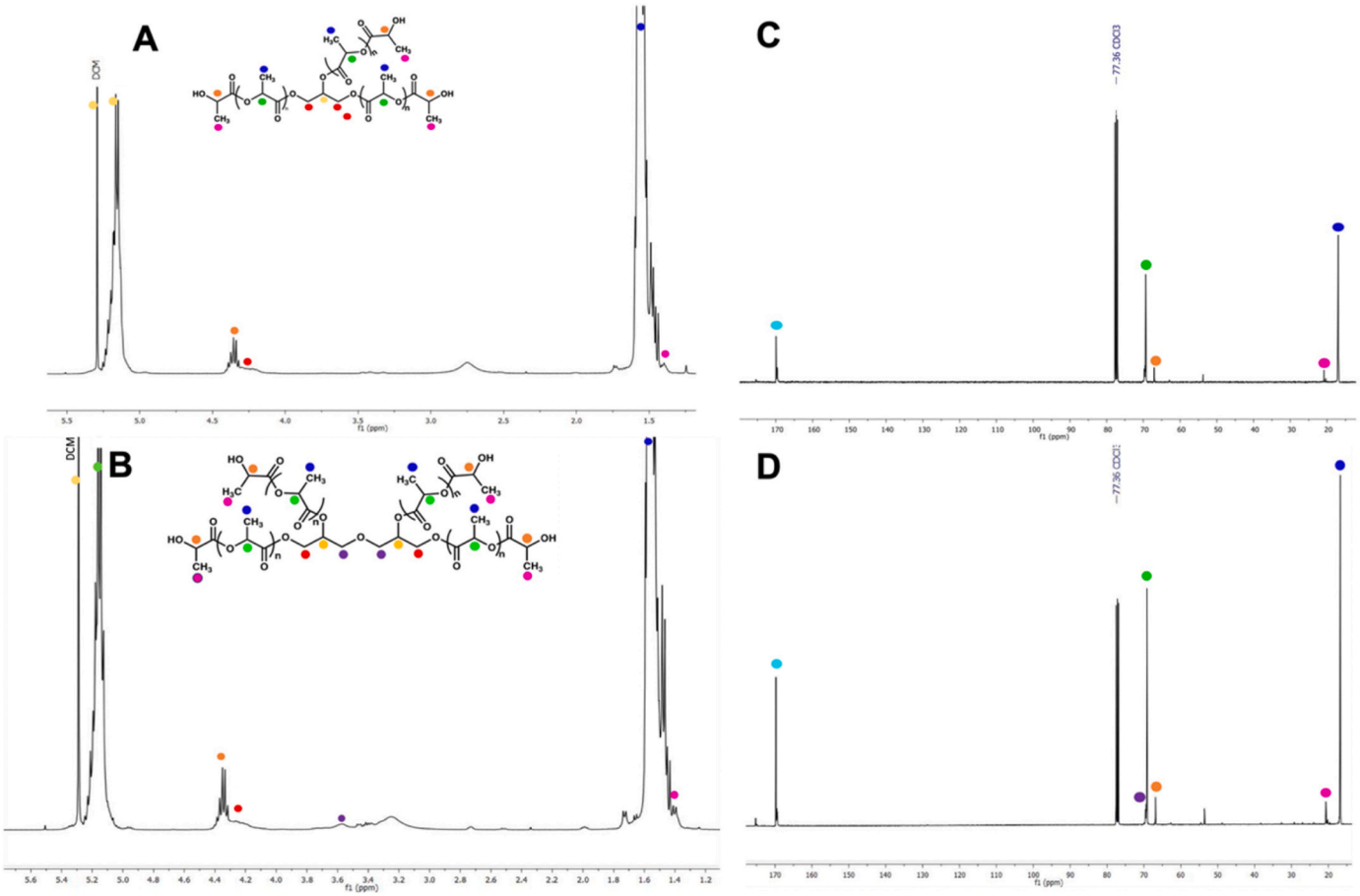

Fig. 1. ^{1}H NMR of Gly-PLLA8 (A) and DGly-PLLA8 (B); ^{13}C NMR spectra of Gly-PLLA8 (C) and DGly-PLLA8 (D).

not observed in the NMR spectra of the longer chain length glycerol-based polymers, indicating that 1,2,3-trisubstitution is more prevalent in those systems (Fig. S2) [27].

Two-dimensional $^{1}H–^{13}C$ HSQC NMR spectroscopy was used to establish one-bond correlations between proton and carbon resonances, enabling unambiguous signal assignment of the polymer backbone and end-group functionalities (Fig. S9).

While initially observed in the DGly-PLLA8 polymer, the HSQC cross peak at 5.32 and 69.79 ppm (Fig. S9A), corresponding to substitution at the secondary hydroxyl group, is no longer detectable in higher molar mass polymers prepared at increased monomer to initiator ratios (Fig. S9B and S9C) [28].

For all samples, the experimental degree of polymerization $DP_{n,\mathrm{exp}}$ was found to be lower than the theoretical degree of polymerization ($DP_{n,\mathrm{th}}$), for both Gly and DGly initiator. This discrepancy can be attributed to the presence of small amounts of residual impurities acting as unintended initiators, which, despite extensive purification of the reagents, may still be present in the reaction mixture, compared to the actual target reagents that should commence the polymerization. In addition, the conversion in all cases was not complete. The monomer conversion was calculated from the $DP_{n,\mathrm{exp}}/DP_{n,\mathrm{th}}$ ratio (Table 1) and ranged from 50 to 80%.

In Table 1, the number average molar mass as determined by GPC ($M_{n,\ GPC}$) is also reported. Conventional GPC calibrated with linear PMMA standards provides only an apparent molecular weight for star-shaped PLLA, as separation is based on hydrodynamic volume rather than true mass and does not account for the more compact conformation of branched architectures. $M_{n,NMR}$ and $M_{n,GPC}$ differ primarily in that NMR provides an absolute number-average molar mass by comparing end-group signals to those of the repeating units. Thus, this measurement is governed by stoichiometry and not linked to hydrodynamic volume.

The obtained dispersity ($Đ$) values of the star-shaped polymers are coherent with a branched topology, especially for the Gly series, where the structural complexity common in star polymer syntheses can manifest as broadened dispersity or apparently monomodal peaks that are not structurally resolved by refractive index detection alone. This effect is further exacerbated by architectural factors that influence polymer solvation and may promote weak interactions with the column matrix, thereby distorting the ideal size-based separation.

The star-shaped Gly-PLLA8 exhibits a lower GPC-determined molar mass ($M_{n,\mathrm{GPC}}$) than the linear lin-PLLA24, although they have similar $M_{n,\mathrm{NMR}}$. This behavior is consistent with the branched architecture of the star polymer, which is characterized by a smaller hydrodynamic radius compared to linear chains [29], as confirmed by SAXS data (Fig. 2A andG).

3.2. SAXS analysis

SAXS measurements were performed on solutions of the synthesized PLLA polymers (10 mg/mL) in acetone, with THF used only for Gly-PLLA24 and DGly-PLLA24 samples (Fig. 2, S10; Table S1).

For low-molar-mass polymers ($M_{n,\mathrm{GPC}}$<6 kDa, Fig. 2A–C, D) and for polymers soluble in THF (Gly-PLLA24 and DGly-PLLA24) (Fig. 2H and I), the scattering profiles were consistent with single-chain behavior, with pair distance distribution functions P(r) indicating dimensions in the range of 7–11 nm. This confirms that, in this molar mass range, the polymers behave as single dissolved chains. As expected, the radius of gyration (R_g) increased with increasing polymer molar mass in the same solvent. When Gly-PLLA24 was dissolved in THF (Fig. 2H) instead of acetone (Fig. 2C), a more expanded chain conformation was observed, as evidenced by an increased R_g and a Porod exponent below 2 (excluded volume parameter = 1/Porod exponent >0.5), suggesting enhanced solvation in THF.

Polymers showing intermediate molar mass, $M_{n,\mathrm{GPC}}$ between 6 and 12 kDa (lin-PLLA24, Gly-PLLA16, and DGly-PLLA16), after an initial dissolution in acetone, turned opalescent after two months stored at 4 °C. In these latter cases, the SAXS profiles displayed a high scattering intensity in low q region with an initial slope at q^{-2} (Fig. S10), indicating larger scale correlations and possibly the formation of large (>100 nm) aggregates, coherently with the opalescent appearance. The power law observed in the low q region suggests a local planar geometry for the large species, which can be attributed to vesicles, modeled as lamellar objects with a thickness of approximately 12 nm (Fig. 2B–E, and G). The highest molar mass polymer DGly-PLLA24 ($M_{n,\mathrm{GPC}}$ ~20 kDa) similarly displayed a high scattering intensity in low q region with an initial slope at q^{-2} in acetone (Fig. 2F) but the scattering profile was consistent with single-chain behavior when solubilized in THF (Fig. 2I).

3.3. Thermal properties

DSC curves of polymers are reported in Fig. 3. As expected, linear PLLA exhibited a semicrystalline behavior with a glass transition temperature (T_g) of ca. 40 °C, crystallization (T_c) at ca. 110 °C and melting (T_m) at 150 °C. The degree of crystallinity χ_c in this sample resulted to be ca. 25%.

By comparison, star-shaped polymers, expect for DGly-PLLA24, were found to be amorphous, exhibiting T_g in the range of 35-50 °C, which is consistent with the presence of branching [1]. A general increase in T_g was observed with increase in arm length (Table S2), reflecting reduced segmental mobility and a diminished contribution of chain-end effects. When the molar mass was similar, e.g. lin-PLLA24 and Gly-PLLA8, the star-branched Gly-PLLA8 exhibited a lower T_g (Table S2), likely due to increased free volume arising from the branched architecture [5].

There was one exception to this, where the DGly-PLLA24 demonstrated semicrystalline behaviour. The characteristic transition temperatures are generally higher than lin-PLLA24 (T_g = 50 °C, T_c = 118 °C and T_m = 160 °C). Also, χ_c was higher, ca. 35%. Similar to the linear sample, two melting peaks are observed, which can be attributed to melting and recrystallization phenomena during heating or the presence of crystals with different morphologies in terms of lamellar thickness or size.

It is known that PLLA can exhibit crystallinity at molar mass as low as 2500 g/mol because of the high chain mobility [30]. Therefore, the

Table 1
Presentation of the $DP_{n,\mathrm{exp}}$ and M_n data for the lin-PLLA24, Gly-PLLA*n* and DGly-PLLA*n* materials.

Sample name	OH Initiator	$DP_{n,\mathrm{th}}$	$DP_{n,\mathrm{exp}}$ [a]	*Conversion* (%)	$M_{n,\mathrm{th}}$ (g/mol)	$M_{n,\mathrm{NMR}}$ (g/mol)	$M_{n,\mathrm{GPC}}$ [b] (g/mol)	$Đ$
lin-PLLA24	1	48	25.5	53	3561	1941	12000	1.4
Gly-PLLA8	3	16	11	69	3545	2465	4200	1.6
Gly-PLLA16	3	32	20.8	66	7000	4582	6000	2.4
Gly-PLLA24	3	48	24.5	50	10457	5384	5700	2.5
DGly-PLLA8	4	16	13.2	81	4770	3964	4100	1.9
DGly-PLLA16	4	32	20	63	9378	5590	9200	1.7
DGly-PLLA24	4	48	36.3	76	13986	10616	20000	1.7

[a] Determined by ^{1}H NMR.
[b] in PMMA equivalent.

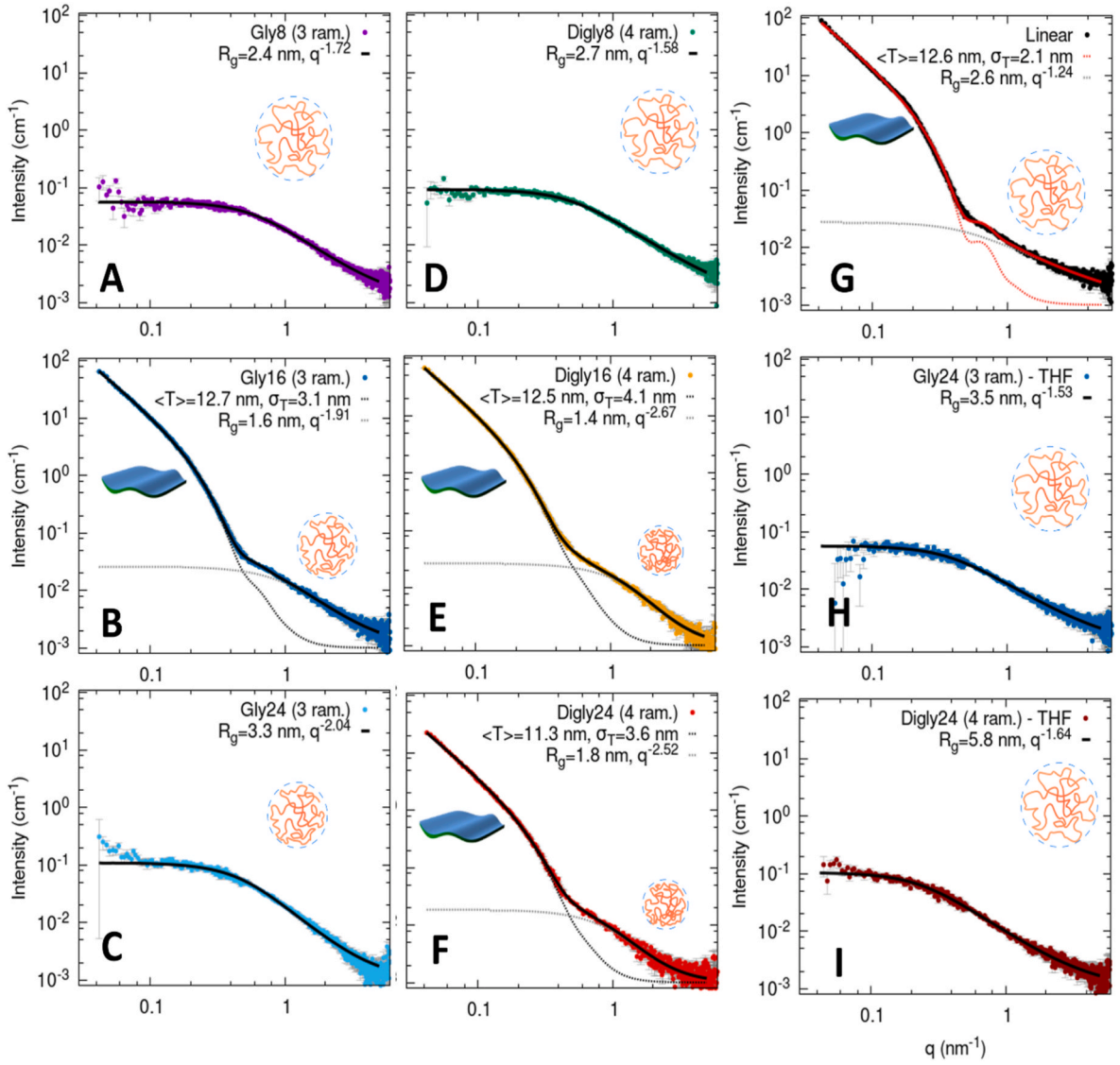

Fig. 2. SAXS analysis of the polymers Gly-PLLA8 (A), Gly-PLLA16 (B), Gly-PLLA24 (C), DGly-PLLA8 (D), Gly-PLLA16 (E), and DGly-PLLA24 (F). Linear PLLA (G) dissolved in acetone at 10 mg/mL and, for Gly-PLLA24 and DGly-PLLA24, also dissolved in THF (H, I) at 10 mg/mL. Experimental scattering profiles on an absolute scale (colored points) and calculated theoretical profiles (solid lines) based on the excluded volume polymer chain model (parameters: radius of gyration Rg, zero-angle scattering intensity I(0), and Porod exponent E for the high-q power law q-E alone, or with the additional contribution of a lamellar aggregate with a Gaussian thickness distribution (mean value <T> and width T). Where the combined polymer and lamellar model was applied, the individual contributions are shown as dashed lines.

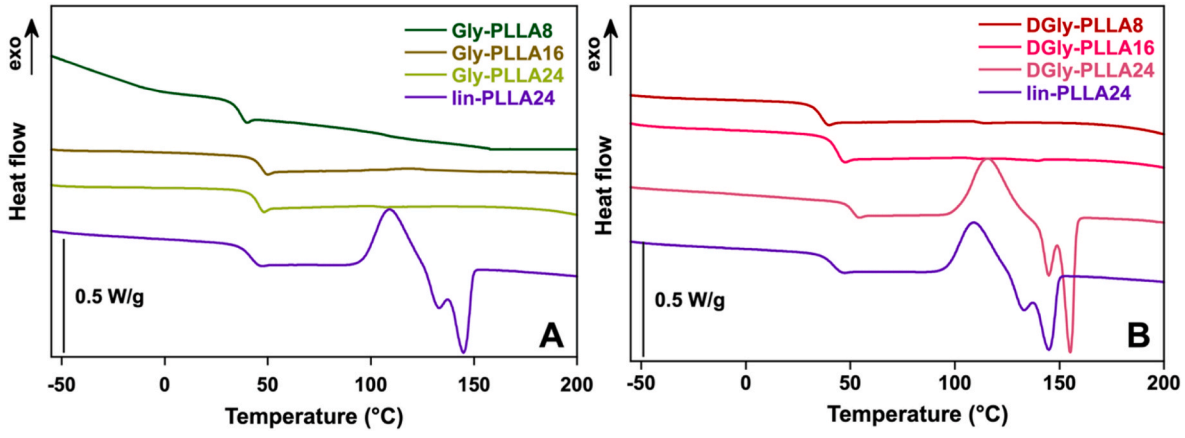

Fig. 3. DSC thermograms of the second heating cycles of Glyn-PLLA (A) and DGlyn-PLLA (B).

observation that among star-shaped samples only DGly-PLLA24 exhibits semicrystalline behavior may be attributed to differences in the spatial arrangement of the initiating hydroxyl groups. In DGly initiator, the closer proximity and steric hindrance of two secondary hydroxyl groups may partially limit chain growth along these arms, thereby favoring more extended growth of the more spatially separated arms, this hypothesis being supported by the lower $Đ$ of DGly-polymers compared to Gly ones as determined by GPC (Table 1). This asymmetric arm development could promote more effective chain packing and crystallization at sufficiently high molecular weights. A similar finding was found by Puchkov et al. [1] who studied the effect of type of polyalcohol initiator on kinetics of L-lactide polymerization. Under the same conditions, rate of initiation of co-initiator's hydroxyl groups varied significantly depending on the structure of the selected alcohol. Specifically, the steric hindrance caused by the structure of the co-initiator molecule was shown to slow down the process of active centers initiation.

The semicrystalline nature of lin-PLLA24 and DGly-PLLA24 was further investigated by POM to analyze the morphology of the polymer crystals (Fig. 4). Upon cooling from the melt to a crystallization temperature of 125 °C, both linear lin-PLLA24 (Fig. 4A and B) and star-shaped DGly-PLLA24 (Fig. 4C and D) exhibited nucleation followed by spherulitic growth, with the number and size of spherulites increasing over time until the field of view was fully covered by crystals. In contrast, Gly-PLLA24 (Fig. 4E and F) did not show any spherulite formation, in agreement with the DSC results. Lin-PLLA24 developed distinct and well-defined spherulites displaying the characteristic Maltese cross extinction pattern, indicative of long-range lamellar order. Conversely, spherulites formed by the star-branched DGly-PLLA24 showed a poorly defined Maltese cross and irregular spherulite edges, suggesting the presence of macroscopic defects in the PLLA spherulites. Such contrast reduction in the spherulites is attributable to the decreased orientation of lamellae and has been observed for L-lactide copolymers with D-lactide [24]. In both lin-PLLA24 and DGly-PLLA24, the length of spherulite radius increased linearly with time evidencing that crystallization rate (G) was constant (Fig. S11A). However, the introduction of branching reduced the crystal growth rate (G) by approximately half, from about 8.2 to 4.5 μm min^{-1} of lin-PLLA24 and DGly-PLLA24, respectively (Fig. S11B).

To explain this behaviour, it was proposed that the more compacted star structure imposes restriction on chain mobility, so weakens the

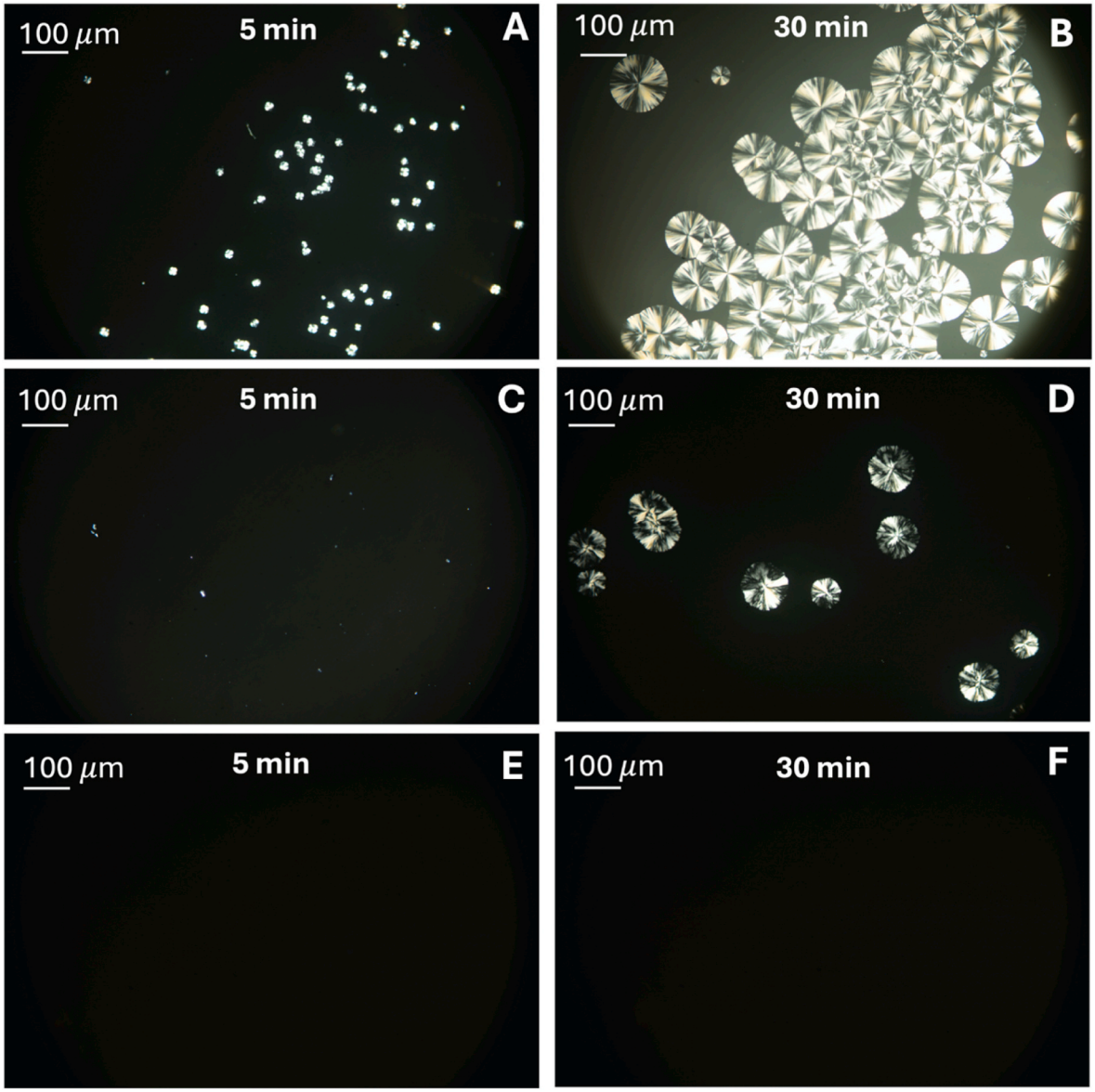

Fig. 4. POM micrographs of lin-PLLA24 (A,B), star-shaped DGly-PLLA24 (C,D) and star-shaped Gly-PLLA24 (E,F) after isothermal melt-crystallization at T = 125 °C.

growth effect to some extent, as has been previously reported for star-comb PLLA structures [29]. In star-shaped PLLAs, the core of the star and the chain ends cannot be efficiently incorporated into the crystalline lattice, remaining in the amorphous phase or at the lamellar interfaces, while arm entanglements can suppress longitudinal chain motions and hinder the reeling-in mechanism during crystal growth. These architectural constraints lead to slower spherulite growth and may increase lamellar surface stresses, this promoted lamellar twisting and resulting in less regular spherulitic morphologies (not defined Mass cross, irregular edges) [31,32].

Thermal degradation profiles of polymers reflected the influence of polymer structure and molar mass on thermal stability (Fig. S12). An initial mass loss observed around 100 °C is attributed to the evaporation of residual adsorbed water. Notably, polymers initiated with DGly display a slightly higher water content compared to the Gly-based polymers (averagely 15% vs 10%), which can be ascribed to the higher density of polar hydroxyl chain-end groups in the DGly series.

Upon further heating, thermal degradation proceeds through concurrent ester hydrolysis, random backbone scission, and intra- or intermolecular transesterification reactions. Star-shaped PLLA exhibited lower degradation temperatures (T_d) compared to lin-PLLA24 (Fig. S13A and B), which can be attributed to the higher density of reactive chain ends in the multi-arm architecture, promoting backbiting and "zip-like" depolymerization [33]. Within the DGly series, T_d increased with molar mass (Fig. S13B). This observation is consistent with DSC results, where partial crystallinity was detected for DGly-PLLA24 and attributed to the preferential growth of the spatially separated arms in the four-arm architecture. In contrast, the Gly-series lacks this structural arrangement, exhibits amorphous behavior, and therefore shows no clear dependence of T_d on molecular weight (Fig. S13A).

3.4. Self-assembly of polymers

To study polymer self-assembling, aggregation in water was induced by nanoprecipitation in absence of surfactants. The size distribution curves determined by DLS are shown in Fig. 5, while the hydrodynamic diameters, PDI and ζ-potential are summarized in Table 2.

The size distribution curves were generally monomodal, with hydrodynamic diameters ranging from 140 to 210 nm and low polydispersity indices (PDI <0.2), indicating good colloidal homogeneity. DGly-based nanosystems exhibiting larger sizes than their Gly-based counterparts. This behavior may suggest a less compact structure together with a higher hydrophilicity of DGly-derived polymers, arising from the increased number of hydroxyl chain-end groups. Notably, lin-PLLA24 and DGly-PLLA24 nanosystems formed the smallest nanoparticles, 160 nm and 140 nm, respectively, which was thought to be lined to reflecting the polymers' tendency toward intrinsic semicrystalline structures formation in the solid state.

To assess whether the semicrystallinity observed in bulk lin-PLLA24 and DGly-PLLA24 is preserved after nanoparticle formation, FTIR and DSC analyses were performed on dried nanoparticle powders of lin-PLLA24, Gly-PLLA24, and DGly-PLLA24 (Fig. S14). The amorphous Gly-PLLA24 was included as a negative control. The FTIR spectra (Fig. S14A and B) display conformational bands associated with torsional angles around single bonds, as well as bands related to conformational regularity along the polymer chain. These regularity bands arise from the coupling of vibrational modes of repeating units and are characteristic of semicrystalline phases, disappearing upon polymer melting. In particular, the band at 918 cm^{-1} is attributed to a helical structure composed of sequential (gauche/trans) (gt) conformers [34]. Notably, this band is absent in all nanoparticle samples, indicating that the semicrystalline organization present in the bulk polymers is not retained following nanoprecipitation. DSC analysis further supports the amorphous nature of the nanoparticle systems. During the first heating

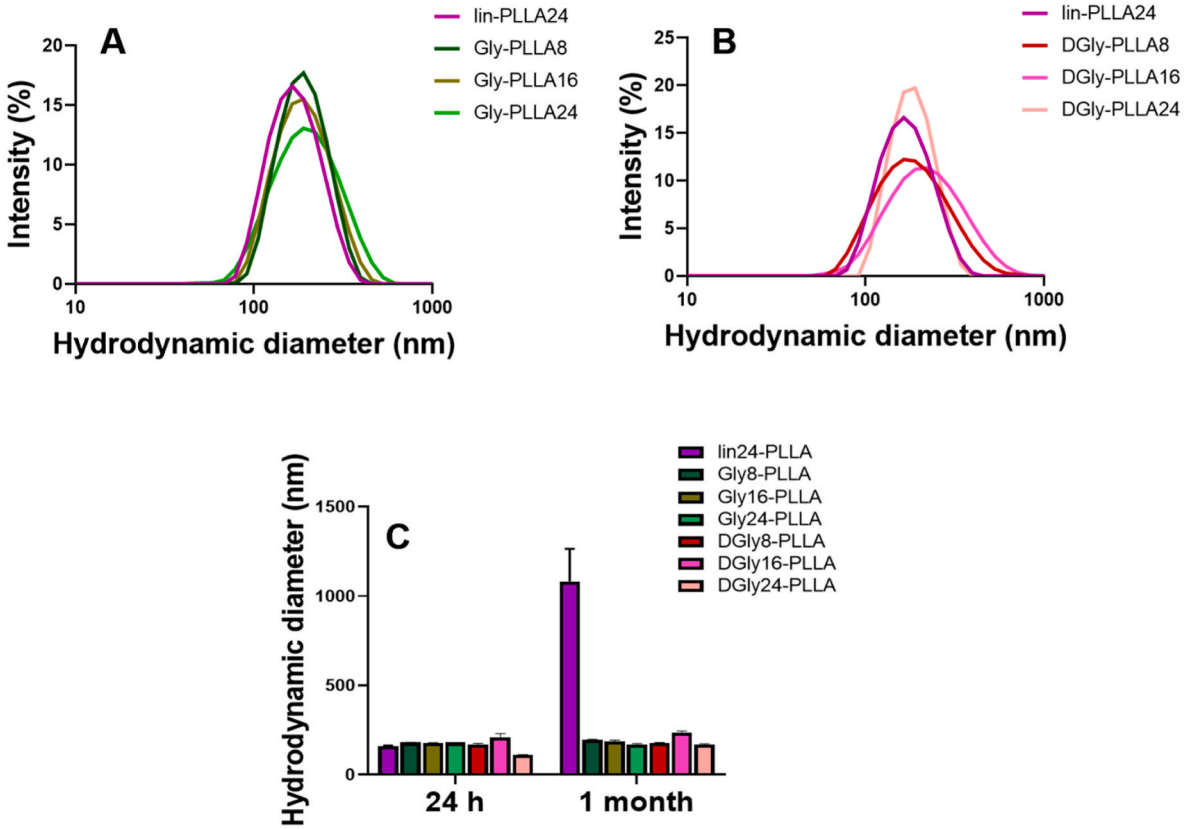

Fig. 5. DLS curve comparison between lin-PLLA24, Gly-PLLAn (A) and DGly-PLLAn (B). Average size of plain polymer aggregates in water at 24 h and 1 month (C).

Table 2
Average size, polydispersity index (PDI), and ζ-potential of the polymers before and after encapsulation.

Sample	Unloaded polymer nanoaggregates			UA-loaded polymer nanoaggregates		
	Hydrodynamic diameter (nm)	PDI	ζ-potential (mV)	Hydrodynamic diameter (nm)	PDI	ζ-potential (mV)
lin-PLLA24	161 ± 2	0.100 ± 0.03	−19.4 ± 1.8	380 ± 40	0.4 ± 0.1	−13.5 ± 3.5
Gly-PLLA8	180 ± 2	0.070 ± 0.01	−28.2 ± 0.7	217 ± 10	0.3 ± 0.03	−24.5 ± 1.2
Gly-PLLA16	177 ± 1	0.105 ± 0.01	−23.7 ± 0.6	202 ± 6	0.32 ± 0.03	−21.4 ± 2.1
Gly-PLLA24	180 ± 1	0.139 ± 0.01	−25.6 ± 0.9	217 ± 8	0.41 ± 0.02	−35.3 ± 3.0
DGly-PLLA8	169 ± 6	0.178 ± 0.02	−25.4 ± 1.0	260 ± 40	0.28 ± 0.03	−27.8 ± 3.5
DGly-PLLA16	210 ± 20	0.260 ± 0.06	−26.4 ± 0.7	190 ± 7	0.28 ± 0.03	−29.9 ± 2.9
DGly-PLLA24	140 ± 1	0.100 ± 0.01	−27.0 ± 2.0	196 ± 2	0.16 ± 0.01	−32 ± 1

scan, both lin-PLLA24 and DGly-PLLA24 nanoparticles exhibit a pronounced cold crystallization peak, followed by a melting transition in the 150–170 °C range. Overall, the smaller nanoparticle size observed for lin-PLLA24 and DGly-PLLA24 may be attributed to a poor swelling ability of these polymers in water.

All samples exhibited a negative ζ-potential. This negative surface charge is primarily attributed to the preferential adsorption of hydroxyl anions from the aqueous phase onto the nanoparticle interface, a behavior commonly observed for or PEGylated nanoparticles [35]. Beyond ion adsorption, the negative surface charge is likely reinforced by the dipolar orientation of water molecules around the dense terminal hydroxyl groups of the glycerol/diglycerol units. The hydrogen-bonding network at the interface creates a structured hydration shell with a specific dipolar alignment, providing additional stability to the nanoparticles.

Polymer nanoaggregates morphology was observed by FESEM (Fig. S15). All the obtained samples exhibited the tendency to aggregate because of the solvent evaporation. Specifically, lin-PLLA24 and DGly-PLLA24 showed a discrete distribution of spherical nanoparticles, with size ranging from 100 to 200 nm, coherent with DLS measurements (Figure S15 A,D,G). At high magnification images (100 KX), DGly-PLLA24 revealed a superior degree of structural complexity, with the formation of multi-directional clusters. Instead, the branched Gly-PLLA24 showed morphological heterogeneity with the coexistence of spherical nanoparticles and elongated, interconnected structures (Figure S15 B,E,H).

The colloidal stability of the NPs in water was studied by monitoring size change over time by DLS (Fig. 5C). Specifically, lin-PLLA24 exhibit a strong tendency to aggregate over time, reaching a size of over one micron after one month. Contrarily, the dimensions of star-shaped PLLAs remain nearly constant for up to one month, suggesting that star-shaped architecture enhances colloidal stability, presumably by promoting a more uniform formation of hydrophilic shell.

3.5. Capability to achieve encapsulation

Encapsulation efficiency of a hydrophobic probe was assessed to investigate how polymer architecture influences nanoscale organization and core compactness of the resulting nanoparticles. To this aim, we selected UA as hydrophobic compound, which has also relevant biological properties [36]. This drug is known to be hepatotoxic, and its encapsulation may reduce cytotoxicity and increase bioavailability. Distribution curves of polymer nanoaggregates after encapsulation of the hydrophobic probe UA are reported in Fig. 6 while dimensions and

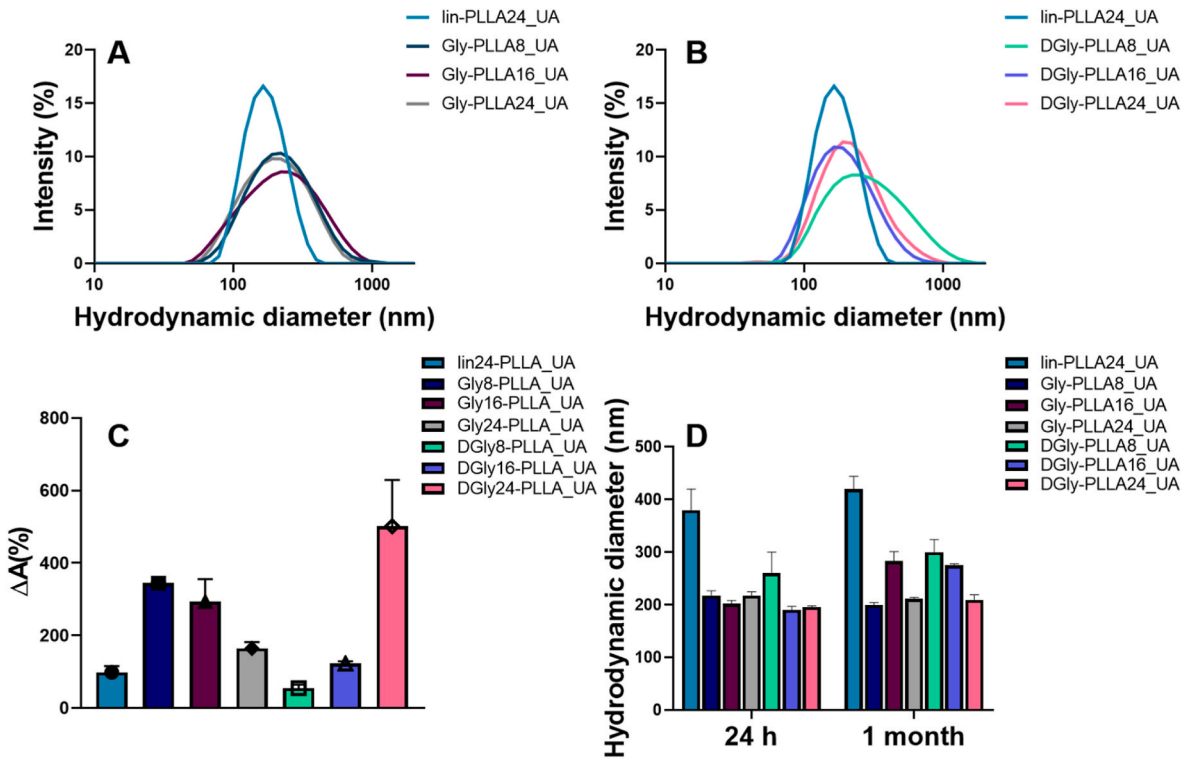

Fig. 6. DLS curves of UA-loaded lin-PLLA24, Gly-PLLAn (A) and DGly-PLLAn (B); Apparent solubility (ΔA%) of loaded lin-PLLA, Gly-PLLAn and DGly-PLLAn (C); Average size of UA-loaded polymer aggregates in water at 24 h and 1 month (D).

ζ-potential values are reported in Table 2.

In general, size distribution curves of UA-loaded nanoaggregates were monomodal (Fig. 6A and B) but broader compared to unloaded aggregates, showing PDI ≥ 0.2 (Table 2) and negative ζ-potential values. Particle size remained essentially unchanged in all systems after 1 month (Fig. 6D).

The amount of encapsulated UA, estimated from apparent solubility measurements (Fig. 6C), revealed a marked difference between lin-PLLA24 and the star-shaped nanosystems. Within the amorphous Gly-based systems, a progressive decrease in the apparent solubility of UA was observed with increasing arm molar mass. We hypothesize that this behavior is related to chain entanglements, which increase polymer packing density and reduce free volume. As a result, the star-shaped polymers behave as compact, globular structures, where UA adsorption occurs primarily at the surface. The increase in molar mass enlarges these spheres, decreasing the surface-to-volume ratio available for adsorption.

This trend was not observed for the DGly-based PLLA systems, which displayed the opposite behavior, where encapsulation efficiency increased with arm length. The best performing sample was DGly-PLLA24_UA, for which the UA solubility in water increased up to 500 times compared to the free drug. This distinct response can result from the asymmetric growth of DGly-based PLLAs, previously hypothesized, where steric hindrance of the DGly core favors elongation along the more spatially separated arms. Such growth may produce a less dense/more open, accessible outer shell. As the molar mass increases, the elongating arms thicken the shell, increasing the fraction of hydrophobic domains available for guest-molecule encapsulation.

The hypotheses are further supported by examining the physical state, amorphous or crystalline, of the encapsulated UA (Fig. S16). UA is a crystalline compound, with a melting point at 204 °C (Fig. S16C). UA-loaded polymer samples (Fig. S16A and B) exhibited the characteristic glass transition of PLLA, in the 40–50 °C range, together with additional crystallization (70–100 °C) and melting (180–190 °C) transitions associated with the encapsulated UA (Table 3). In the star-shaped systems, the UA melting enthalpy (ΔH_m) was consistently higher than its crystallization enthalpy (ΔH_c), suggesting that UA was present in both crystalline and amorphous states. The fraction of amorphous UA crystallizing upon heating was estimated from the $\Delta H_c/\Delta H_m$ ratio and is reported in Table 3. Except for lin-PLLA24, the amorphous fraction exceeded 50% and reached values above 90% in the DGly-PLLA16 and DGly-PLLA24 samples. These results highlight the critical role of polymer architecture in governing the physical state and organization of the encapsulated guest molecule, with star-shaped architectures favoring amorphous stabilization within the polymer matrix.

The amorphous UA fraction in Gly-series lower than DGly-series suggests that drug incorporation occurs mostly at the polymer surface rather than within the bulk. In contrast, the almost complete amorphization of UA, even in partially crystalline polymer DGly-PLLA24, supports the hypothesis of a drug intimately dispersed in hydrophobic shell that stabilizes the drug. Therefore, the polymer architecture not only affected the level of molecular encapsulation but also its organization within the system.

3.6. Effects of UA-loaded nanosystems on cells

Encapsulation of hydrophobic compounds in polymer systems is particularly relevant in biomedical field, since many active pharmaceutical ingredients are hydrophobic. This is the case of UA, which despite its limited bioavailability, has attracted increasing attention in recent years for its potential antitumor properties, particularly against solid tumors. In the present context, available experimental evidence supports its ability to inhibit cancer cell proliferation through multiple mechanisms, including mitochondrial dysfunction, induction of oxidative stress, and modulation of cell cycle progression [37]. These effects appear to be especially relevant in highly proliferative solid tumors, such as breast cancer, where metabolic vulnerability represents a key therapeutic target [38]. However, despite the promising antitumoral properties, the clinical translation of UA is significantly limited by its toxicity profile [39]. Hepatotoxicity represents the most critical adverse effect, with several studies reporting dose-dependent liver injury associated with mitochondrial uncoupling and impaired oxidative phosphorylation [40]. This toxic effect is not restricted to cancer cells and raises concerns regarding the therapeutic window of UA. Furthermore, systemic toxicity has been observed in both *in-vitro* and *in-vivo* models, highlighting the lack of selectivity between malignant and normal tissues at higher concentrations [41,42].

For these reasons, we focused on the encapsulation of UA into DGly-PLLA24 nanosystems to achieve a more controlled and targeted release toward tumor cells, while preserving its therapeutic activity. UA encapsulation into nanoparticles is expected to improve bioavailability and tumor selectivity, mitigating the dose-dependent toxic effects associated with free UA while maintaining its antitumoral efficacy against breast cancer cells.

Triple-negative breast cancer MDA-MB-231 cells were exposed to three different concentrations of free UA: 58, 29, and 14.5 μM. The concentrations were selected based on literature data, observing an IC_{50} value of approximately 29 μM for this cell line, and a dose-dependent cytotoxic effect with free UA (Fig. 7A). In parallel, UA-loaded DGly-PLLA24 systems were tested at concentrations containing the same amounts of free UA. Compared to unencapsulated UA, the DGly-PLLA24 containing UA exhibited reduced cytotoxic activity. Even at the highest concentration tested (58 μM), only a slight reduction in cell viability was observed; however, this effect was not statistically significant. Additionally, empty nanoparticles were evaluated at concentrations equivalent to those used for UA-loaded systems and showed no detectable cytotoxicity, confirming their biocompatibility in MDA-MB-231 cells. This result could suggest a more controlled interaction with MDA-MB-231 cells, potentially allowing selective drug release while limiting non-specific toxicity.

Integrins play a crucial role in breast cancer progression by mediating cell–extracellular matrix interactions, thereby regulating key processes such as cell adhesion, migration, invasion, and survival. In particular, integrin β1 is overexpressed in aggressive breast cancer phenotypes, including triple-negative breast cancer, and is associated with enhanced metastatic potential and poor prognosis [43]. In our experimental condition, free UA was able to decrease the amount of integrin β1, mainly after 24 h treatment as observed in Fig. 7B, respect the untreated cells (CTL) (red fluorescence). Very interestingly,

Table 3
Thermal properties of loaded lin-PLLA24, and star-shaped Gly_n-PLLA and $DGly_n$-PLLA.

Sample	T_g (°C)	ΔC_p (J g^{-1})	UA ΔH_c (mJ)	UA ΔH_m (mJ)	amorphous UA (%)	T_m PLLA (°C)	T_m UA (°C)
lin-PLLA24_UA	48	0.26	74	285	26	146	185
Gly-PLLA8_UA	42	0.27	77	124	62	-	183
Gly-PLLA16_UA	44	0.41	67	107	63	-	184
Gly-PLLA24_UA	46	0.42	148	221	67	-	186
DGly-PLLA8_UA	47	0.31	115	179	64	-	183
DGly-PLLA16_UA	45	0.42	162	178	91	-	185
DGly-PLLA24_UA	48	0.34	189	200	94	151	187

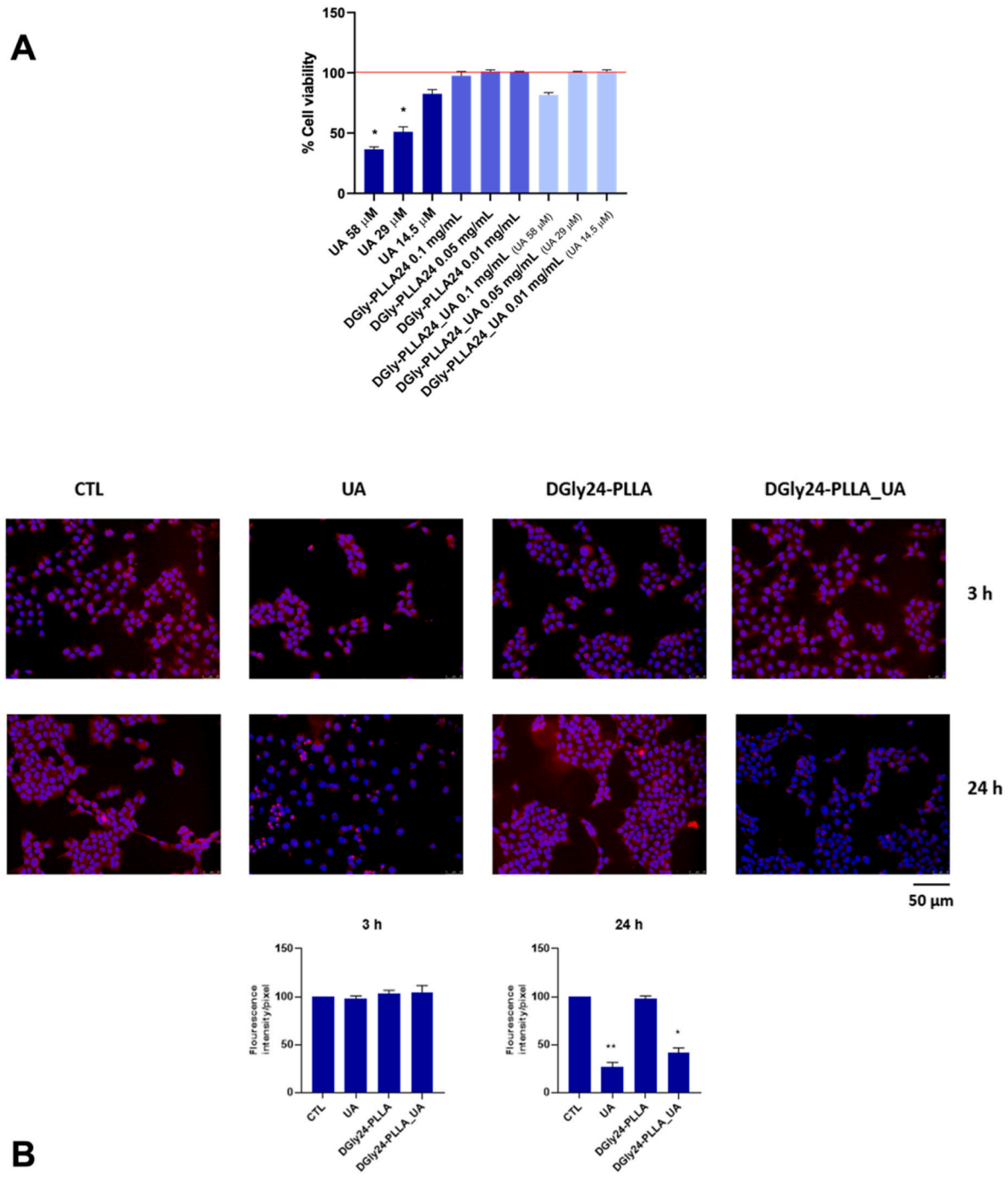

Fig. 7. Cell viability was assessed by the MTS colorimetric method. MDA-MB-231 cells were treated with UA at concentrations of 58, 29, and 14.5 μM, or empty DGly-PLLA24 at 0.1 mg/mL, 0.05 mg/mL and 0.01 mg/mL or DGly-PLLA24_UA at same concentrations of empty DGly-PLLA24 containing 58, 29, and 14.5 μM UA the for 24 h. Cell viability of treated samples was normalized to the untreated cells represented by red horizontal line. *p < 0.05 58 μM and 29 μM UA vs. CTL. (A) Effects of UA, DGly-PLLA24 and DGly-PLLA24_UA treatment on Integrin β1 protein expression. MDA-MB-231 cells, seeded at 5×10^3 cell density, were treated with UA or DGly-PLLA24_UA at UA concentration of 14.5 μM for 3 h and 24 h, and then analysed by immunofluorescence using anti-Integrin β1 primary antibody and Alexa Fluor 594 (red) secondary antibody. Nuclei were stained with DAPI (original magnification 20 ×). The bar graph represents the pixel intensities in the region of interest, obtained by ImageJ, measuring the red fluorescence in 50 fields of each captured picture using exactly the same parameters of exposition, gain and saturation. The results are expressed as mean ± SD of data obtained by three independent experiments. *$p < 0.05$ DGly-PLLA24_UA vs. CTL; **$p < 0.01$ UA vs. CTL. (B). (For interpretation of the references to color in this figure legend, the reader is referred to the Web version of this article.)

UA-encapsulated DGly-PLLA24 NPs were able to significantly reduce integrin β1 protein expression to levels comparable to those observed following treatment with free UA. Furthermore, UA-encapsulated DGly-PLLA24 NPs were not detrimental for cell viability, whereas free UA was very detrimental, as observed in Fig. 7B, considering that the same number of cells was seeded for all treatments (Fig. 7B).

However, in contrast to the unencapsulated molecule, the DGly-PLLA24_UA did not induce evident cytotoxic effects under the same experimental conditions. These effects on integrin β1 expression were detectable after 24 h of treatment, whereas no significant changes were observed at the earlier time point of 3 h (Fig. 7B). In this context, modulation of integrin β1 expression could represent an additional

mechanism underlying the antitumoral effects of UA in MDA-MB-231 breast cancer cells while limiting off-target toxicity.

4. Conclusions

Overall, the results show that beyond a simple linear-to-star comparison, polymer crystallinity, thermal stability, and hydrophobic guest encapsulation is mainly governed by how the core geometry and steric hindrance dictates arm growth and packing. Diglycerol-based asymmetric star architectures obtained at higher molar mass showed higher thermal stability, crystallinity and ability to stabilize amorphous guest molecules compared to glycerol-star polymers. This behavior supports a structural model in which steric hindrance and proximity of hydroxyl groups at the DGly core induce asymmetric arm growth, favoring the development of longer, more extended arms that pack more efficiently and partially crystallize. POM observations, however, showed less regular spherulitic morphologies and lower crystallization rate for the DGly-PLLA24 compared to lin-PLLA24, suggesting restriction on chain mobility imposed by the star architecture.

Gly-based systems increasingly limit guest accommodation with increasing arm length, whereas DGly-PLLA polymers benefit from the asymmetry imposed by DGly core, which may produce a more open structure with an accessible outer shell available for guest-molecule encapsulation.

Biological tests performed on MDA-MB-231 triple-negative breast cancer cells showed that UA encapsulation in diglycerol-star shaped PLLA reduced UA cytotoxicity and integrin β1 protein expression, known to play a crucial role in breast cancer progression. Overall, findings suggest the relevance of these systems for the design of materials for the controlled incorporation of hydrophobic low-molecular-weight compounds in applications such as drug delivery systems, coatings or additive-loading packaging.

CRediT authorship contribution statement

Benedetta Brugnoli: Writing – original draft, Investigation, Funding acquisition, Data curation. **Chiara Frezza:** Methodology, Investigation. **Alessia Mariano:** Writing – review & editing, Methodology, Investigation. **Philippa L. Jacob:** Writing – review & editing, Methodology, Investigation. **Andreas Diacono:** Writing – review & editing, Methodology, Investigation. **Derek Irvine:** Writing – review & editing, Supervision. **Eleni Axioti:** Investigation. **Alessandra Del Giudice:** Writing – review & editing, Funding acquisition, Formal analysis. **Luciano Galantini:** Writing – review & editing, Validation. **Antonella Piozzi:** Writing – review & editing, Validation. **Anna Scotto d'Abusco:** Writing – review & editing. **Vincenzo Taresco:** Writing – review & editing, Supervision, Data curation, Conceptualization. **Iolanda Francolini:** Writing – review & editing, Supervision, Data curation, Conceptualization.

Declaration of competing interest

The authors declare that they have no known competing financial interests or personal relationships that could have appeared to influence the work reported in this paper.

Acknowledgments

I.F., A.D.G. and B.B. wish to thank Sapienza University of Rome (Italy) for supporting the research (project numbers RM1241911257F319 and AR223188B3D95900). I.F. thanks the "Sapienza-Rome Technopole per l'internazionalizzazione della ricerca" PNRR Project ECS 00000024, Rome Technopole-CUP: B83C22002820006 – spoke 1- flagship 7 – task 1 for funding (Italy). P.L.J., A.D., D.J.I. and V. T. thank EPSRC for funding through Prosperity Partnership EP/X025489/1 undertaken in collaboration with Croda (UK). P.L.J. was also supported by an EPSRC Doctoral Prize Fellowship [EP/W524402/1].

Appendix A. Supplementary data

Supplementary data to this article can be found online at https://doi.org/10.1016/j.polymer.2026.129963.

Data availability

Data will be made available on request.

References

[1] A.A. Puchkov, N.G. Sedush, A.I. Buzin, T.N. Bozin, A.V. Bakirov, R.S. Borisov, S. N. Chvalun, Synthesis and characterization of well-defined star-shaped poly(L-lactides), Polymer 264 (2023) 125573, https://doi.org/10.1016/j.polymer.2022.125573.

[2] J.-F. Lutz, J.-M. Lehn, E.W. Meijer, K. Matyjaszewski, From precision polymers to complex materials and systems, Nat. Rev. Mater. 1 (2016) 16024, https://doi.org/10.1038/natrevmats.2016.24.

[3] D.J.A. Cameron, M.P. Shaver, Aliphatic polyester polymer stars: synthesis, properties and applications in biomedicine and nanotechnology, Chem. Soc. Rev. 40 (2011) 1761–1776, https://doi.org/10.1039/c0cs00091d.

[4] E. Núñez, C. Ferrando, E. Malmström, H. Claesson, U.W. Gedde, Crystallization behavior and morphology of star polyesters with Poly(ε-Caprolactone) arms, J. Macromol. Sci. Part B 43 (2004) 1143–1160, https://doi.org/10.1081/MB-200026519.

[5] E.S. Kim, B.C. Kim, S.H. Kim, Structural effect of Linear and star-shaped Poly(L-lactic acid) on physical properties, J. Polym. Sci. B Polym. Phys. 42 (2004) 939–946, https://doi.org/10.1002/polb.10685.

[6] A. Mittal, N. Aarti, S. Vats, F. Zabihi, K. Achazi, F. Rancan, A. Vogt, R. Haag, S. K. Sharma, Synthesis of C3-symmetric star shaped amphiphiles for drug delivery applications, Soft Matter 20 (2024) 1282–1292, https://doi.org/10.1039/d3sm01388j.

[7] A. Duro-Castano, J. Movellan, M.J. Vicent, Smart branched polymer drug conjugates as nano-sized drug delivery systems, Biomater. Sci. 3 (2015) 1321–1334, https://doi.org/10.1039/c5bm00166h.

[8] S. Corneillie, M. Smet, PLA architectures: the role of branching, Polym. Chem. 6 (2015) 850–867, https://doi.org/10.1039/C4PY01572J.

[9] A. Michalski, M. Brzezinski, G. Lapienis, T. Biela, Star-shaped and branched polylactides: synthesis, characterization, and properties, Prog. Polym. Sci. 89 (2019) 159–212, https://doi.org/10.1016/j.progpolymsci.2018.10.004.

[10] H. Tsuji, T. Miyase, Y. Tezuka, S.K. Saha, Physical properties, crystallization, and spherulite growth of linear and 3-arm poly(L-lactide)s, Biomacromolecules 6 (2005) 244–254, https://doi.org/10.1021/bm049552q.

[11] Q. Hao, F. Li, Q. Li, Y. Li, L. Jia, J. Yang, Q. Yang, Q. Fang, A. Cao, Preparation and crystallization kinetics of new structurally well-defined star-shaped biodegradable poly(L-lactide)s initiated with diverse natural sugar alcohols, Biomacromolecules 6 (2005) 2236–2247, https://doi.org/10.1021/bm050213m.

[12] T. Biela, A. Duda, H. Pasch, K. Rode, K. Star-shaped poly(L-lactide)s with variable numbers of hydroxyl groups at polyester arms chain-ends and directly attached to the star-shaped core—Controlled synthesis and characterization, J. Polym. Sci. Polym. Chem. 43 (2005) 6116–6133, https://doi.org/10.1002/pola.21035.

[13] Y. Sakamoto, H. Tsuji, Crystallization behavior and physical properties of linear 2-arm and branched 4-arm poly (l-lactide) s: effects of branching, Polymer 54 (9) (2013) 2422–2434, https://doi.org/10.1016/j.polymer.2013.02.044.

[14] M. Sahranavard, M. Shahriari, K. Abnous, F. Hadizadeh, S.M. Taghdisi, R. Zolfaghari, M. Ramezani, M. Alibolandi, Design and synthesis of targeted star-shaped micelle for guided delivery of camptothecin: in vitro and in vivo evaluation, Mater. Sci. Eng. C 131 (2021) 112529, https://doi.org/10.1016/j.msec.2021.112529.

[15] Y. Zhang, M. Fang, Z. Tan, Y.A. Zhang, C.Y. Huang, L. Lu, J. Tian, L. Li, C. Zhou, Fabrication of an injectable Star-polylactide/Thiolated hyaluronate hydrogel as a double drug-delivery System for cancer treatment, ACS Omega 8 (2023) 16789–16799, https://doi.org/10.1021/acsomega.3c00270.

[16] J. Burke, R. Donno, R. D'Arcy, S. Cartmell, N. Tirelli, The Effect of Branching (Star Architecture) on Poly(d, l -lactide) (PDLLA) Degradation and Drug Delivery, Biomacromolecules 18 (2017) 728–739, https://doi.org/10.1021/acs.biomac.6b01524.

[17] V. Fakhri, C.H. Su, M. Tavakoli Dare, M. Bazmi, A. Jafari, V. Pirouzfar, Harnessing the power of polyol-based polyesters for biomedical innovations: synthesis, properties, and biodegradation, J. Mater. Chem. B 11 (2023) 9597–9629, https://doi.org/10.1039/d3tb01186k.

[18] B. Brugnoli, A. Mariano, B. Simonis, C. Bombelli, S. Sennato, A. Piozzi, V. Taresco, V.M. Chauhan, S.M. Howdle, A. Scotto d'Abusco, I. Francolini, Self-assembled chitosan-sodium usnate drug delivery nanosystems: synthesis, characterization, stability studies, in vitro cytotoxicity and in vivo biocompatibility against 143 B cells, Carb. Polym. Technol. Appl. 6 (2023) 100373, https://doi.org/10.1016/j.carpta.2023.100373.

[19] K.I. Ingoífsdóttir, Molecules of Interest Usnic acid, Phytochem 61 (7) (2002) 729–736.

[20] K. Manalastas, P.V. Konarev, N.R. Hajizadeh, A.G. Kikhney, M.V. Petoukhov, D. Molodenskiy, A. Panjkovich, H.D. Mertens, A.Y. Gruzinov, C. Borges, C. M. Jeffries, D.I. Svergun, D. Franke, Atsas 3.0: expanded functionality and new tools for small-angle scattering data analysis, J. Appl. Cryst. 54 (2020) 343–355, https://doi.org/10.1107/S1600576720013412.
[21] N.K. Abayasinghe, S. Glaser, K. Prasanna, U. Perera, D.W. Jr. Smith, Oligoethylene-end-capped polylactides, J. Polym. Sci. Polym. Chem. 43 (2005) 5257–5266, https://doi.org/10.1002/pola.20889.
[22] J.E. Báez, Á. Marcos-Fernández, P. Galindo-Iranzo, Exploring the effect of alkyl end group on poly (L-lactide) oligo-esters. Synthesis and characterization, J. Polym. Res. 18 (5) (2011) 1137–1146, https://doi.org/10.1007/s10965-010-9517-y.
[23] P.L. Jacob, B. Brugnoli, A. Del Giudice, H. Phan, V.M. Chauhan, L. Beckett, R. B. Gillis, C. Moloney, R.J. Cavanagh, E. Krumins, M. Reynolds-Green, J.C. Lentz, C. Conte, V. Cuzzucoli Crucitti, B. Couturaud, L. Galantini, I. Francolini, S. M. Howdle, V. Taresco, Poly (diglycerol adipate) variants as enhanced nanocarrier replacements in drug delivery applications, J. Colloid Interface Sci. 641 (2023) 1043–1057, https://doi.org/10.1016/j.jcis.2023.03.124.
[24] B. Brugnoli, G. Perna, S. Alfano, A. Piozzi, L. Galantini, E. Axioti, V. Taresco, A. Mariano, A. Scotto d'Abusco, S. Vecchio Ciprioti, I. Francolini, Nanostructured Poly-l-lactide and polyglycerol adipate carriers for the encapsulation of usnic acid: a promising approach for hepatoprotection, Polymers 16 (2024) 427, https://doi.org/10.3390/polym16030427.
[25] A.A. Puchkov, N.G. Sedush, A.S. Chirkova, T.N. Bozin, S.N. Chvalun, Synthesis of biodegradable lactide-based polymers in the presence of metal-free organocatalyst, Polym. Sci. Ser. B 65 (2023) 419–428, https://doi.org/10.1134/S1560090423700951.
[26] W. Xie, N. Jiang, Z. Gan, Effects of multi-arm structure on crystallization and biodegradation of star-shaped poly(ε-caprolactone), Macromol. Biosci. 8 (2008) 775–784, https://doi.org/10.1002/mabi.200800011.
[27] V. Taresco, R.G. Creasey, J. Kennon, G. Mantovani, C. Alexander, J.C. Burley, M. C. Garnett, Variation in structure and properties of poly(glycerol adipate) via control of chain branching during enzymatic synthesis, Polymer 89 (2016) 41–49, https://doi.org/10.1016/j.polymer.2016.02.036.
[28] Y. Lin, A. Zhang, Synthesis and characterization of star-shaped poly(d,l-lactide)-block- poly(ethylene glycol) copolymers, Polym. Bull. 65 (2010) 883–892, https://doi.org/10.1007/s00289-010-0252-7.
[29] X. Leng, Z. Wei, Y. Ren, Y. Li, Y. Wang, Q. Wang, Facile synthesis and comparative study of poly(l-lactide) with linear-comb and star-comb architecture, RSC Adv. 5 (2015) 81482–81491, https://doi.org/10.1039/C5RA15141D.
[30] M. Brzezinski, T. Biela, Supramolecular polylactides by the cooperative interaction of the end groups and stereocomplexation, Macromolecules 48 (9) (2015) 2994–3004, https://doi.org/10.1021/acs.macromol.5b00208.
[31] H. Tsuji, Y. Ikada, Crystallization from the melt of poly(lactide)s with different optical purities and their blends, Macromol. Chem. Phys. 197 (1996) 3483–3499, https://doi.org/10.1002/macp.1996.021971033.
[32] J. Bojda, E. Piorkowska, G. Lapienis, A. Michalski, Crystallization of star-shaped and linear poly(L-lactide)s, Eur. Polym. J. 105 (2018) 126–134, https://doi.org/10.1016/j.eurpolymj.2018.05.017.
[33] F. Carrasco, J. Cailloux, P.E. Sánchez-Jiménez, M.L. Maspoch, Improvement of the thermal stability of branched poly(lactic acid) obtained by reactive extrusion, Polym. Degrad. Stab. 104 (2014) 40–49, https://doi.org/10.1016/j.polymdegradstab.2014.03.026.
[34] Z. Zhu, Y. Bian, X. Zhang, R. Zeng, B. Yang, Study of cristallinity and conformation of Poly(Lactic acid) by Terahert Spectroscopy, Anal. Chem. 94 (31) (2022) 11104–11111, https://doi.org/10.1021/acs.analchem.2c02652.
[35] S. Zaichik, C. Steinbring, M. Jelkmann, A. Bernkop-Schnürch, Zeta potential changing nanoemulsions: impact of PEG-corona on phosphate cleavage, Int. J. Pharm. 581 (2020), https://doi.org/10.1016/j.ijpharm.2020.119299.
[36] I. Francolini, P. Norris, A. Piozzi, G. Donelli, P. Stoodley, Usnic acid, a natural antimicrobial agent able to inhibit bacterial biofilm formation on polymer surfaces, Antimicrob. Agents Chemother. 48 (2004) 4360–4365, https://doi.org/10.1128/AAC.48.11.4360-4365.2004.
[37] Eydis Einarsdóttir, Judith Groeneweg, Guðrún G. Björnsdóttir, Guðleif Harðardottir, Sesselja Omarsdóttir, Kristín Ingólfsdóttir, Helga M. Ögmundsdóttir, Cellular mechanisms of the anticancer effects of the lichen compound usnic acid, Planta Med. 76 (2010) 969–974.
[38] S. Zuo, L. Wang, Y. Zhang, D. Zhao, Q. Li, D. Shao, X. Fang, Usnic acid induces apoptosis via an ROS-dependent mitochondrial pathway in human breast cancer cells in vitro and in vivo, RSC Adv. 5 (2015) 153–162, https://doi.org/10.1039/C4RA12340A.
[39] L.E.I. Guo, Q. Shi, J.-L. Fang, N.A.N. Mei, A.A. Ali, S.M. Lewis, J.E.A. Leakey, V. H. Frankos, Review of usnic acid and Usnea Barbata toxicity, J. Environ. Sci. Health C 26 (2008) 317–338, https://doi.org/10.1080/10590500802533392.
[40] D. Han, K. Matsumaru, D. Rettori, N. Kaplowitz, Usnic acid-induced necrosis of cultured mouse hepatocytes: inhibition of mitochondrial function and oxidative stress, Biochem. Pharmacol. 67 (2004) 439–451, https://doi.org/10.1016/j.bcp.2003.09.032.
[41] Y. Yokouchi, M. Imaoka, N. Niino, N. Kiyosawa, A. Sayama, T. Jindo, (+)-Usnic acid-induced myocardial toxicity in rats, Toxicol. Pathol. 43 (2015) 424–434, https://doi.org/10.1177/0192623313504308.
[42] I. Prokopiev, G. Filippova, E. Filippov, I. Voronov, I. Sleptsov, A. Zhanataev, Genotoxicity of (+)- and (−)-usnic acid in mice, Mutat. Res. Genet. Toxicol. Environ. Mutagen. 839 (2019) 36–39, https://doi.org/10.1016/j.mrgentox.2019.01.010.
[43] Q. Huang, J. Wang, H. Ning, W. Liu, X. Han, Integrin β1 in breast cancer: mechanisms of progression and therapy, Breast Cancer 32 (1) (2025) 43–59, https://doi.org/10.1007/s12282-024-01635-w.